Received: 31 October 2025 | Revised: 29 January 2026 | Accepted: 23 February 2026

DOI: 10.1002/qj.70169

Quarterly Journal of the Royal Meteorological Society RMetS

RESEARCH ARTICLE

Suggestions for unifying the parametrizations of turbulent orographic form drag, mountain wave drag, and flow blocking

Francois Lott[1] | **Anton Beljaars**[2] | **Bruno Deremble**[3]

[1]Laboratoire de Météorologie Dynamique, Sorbonne Université, PSL/Ecole Normale Supérieure, Paris, France

[2]European Centre for Medium-Range Weather Forecasts, Reading, UK

[3]Institut des Géosciences de l'Environnement, University of Grenoble Alpes, Grenoble, France

Correspondence
Francois Lott, Laboratoire de Météorologie Dynamique, IPSL, Paris, France.
Email: francois.lott@sorbonne-universite.fr

Funding information
Schmidt Sciences, as part of the Virtual EarthSystem Research Institute (VESRI) project DataWave.

Abstract

Parametrizations of subgrid-scale mountains are commonly used in numerical weather prediction and climate models. They try to represent quite separate processes; namely, the enhancement of the turbulent drag by orography, gravity-wave drag, and the effects of low-level flow blocking. Among the gravity wave schemes, some of them distinguish between upward-propagating waves and trapped lee waves. This article makes use of a recent theoretical methodology to propose a formalism that includes all these effects. This theory handles enhanced turbulent drag in the neutral case, gravity waves in the stratified case, and trapped lee waves in the transition. Mountain drag associated with all these processes is estimated analytically, as well as the fraction of the drag that stays within the boundary layer instead of being radiated in the far field. Although the theory used is adapted to gentle hills with small slope, we also try to evaluate the blocked layer depth by combining the sheltering effects that dominate when stratification is small and the blocking effects when stratification is strong.

KEYWORDS

neutral and stratified boundary layers, orographic turbulent and gravity-wave drag, parametrization, trapped lee waves

1 | INTRODUCTION

The impact of small- to medium-scale mountains on atmospheric dynamics has been intensively studied over the last 50 years by two quite distinct communities. The first community studies how mountains modify the turbulent boundary layer (e.g., Beljaars *et al.*, 1987; Jackson & Hunt, 1975), an issue that is central in the context of wind resource modelling (Ayotte, 2008) or dune formation (Charru *et al.*, 2012). The background theory used neutral and idealized boundary-layer closures and analyse how it is modified by small-slope orography (Belcher & Hunt, 1998; Hunt *et al.*, 1988a). In this limit, one can consider linear dynamics providing that the problem is formulated using terrain-following coordinates. This linear problem is nevertheless still extremely involved, and uniform solutions are often obtained via numerical integrations (e.g., Beljaars *et al.*, 1987). These are the basic theories that are adapted to parametrize subgrid-scale orography in weather prediction and climate models, initially by increasing the terrain roughness length (Wood & Mason, 1993). Subsequently, Wood *et al.* (2001) used fully

nonlinear simulations to expand the theory and improve the estimate of the depth over which the mountain drag is deposited. This depth estimate is used to formulate a turbulent orographic form drag (TOFD) parametrization (Beljaars *et al.*, 2004), where the depth over which the drag is deposited becomes related to the horizontal scale of the disturbances. Beljaars *et al.* (2004) also assumed that the TOFD parametrization should only be used for mountains with horizontal scales $L < 5000\,\mathrm{m}$. At these scales, and for incident wind U, one can expect that the advective time-scale L/U is smaller than the inverse of the Brunt–Väisälä frequency N^{-1}. This ensures that the flow behaves according to neutral flow dynamics.

The second community is more focused on mountain dynamical meteorology. It studies the onset of mountain waves, downslope winds, foehn, and trapped waves using theories and models where internal gravity waves control the dynamics, and where the boundary layer is often neglected. The body of theoretical literature on the subject is extremely vast in itself (Durran, 1990). The linear hydrostatic theory yields the development of the earlier orographic gravity-wave drag parametrizations (McFarlane, 1987; Palmer *et al.*, 1986), which were used to reduce systematic westerly biases in the upper troposphere. Since then linear theories have also been used to justify the introduction of low-level drags due to trapped waves; for example, by Tsiringakis *et al.* (2017), and in this article to compensate for missing TOFD in the stable case. Prior to that, low-level drag was also introduced, because most mountains force large-amplitude gravity waves that break at low level (Schär & Durran, 1997) and induce upstream blocking, with the flow contouring the obstacle, as illustrated by Schär and Smith (1993) in the shallow water case. Although low-level wave breaking can be encapsulated in a conventional breaking criterion like in Lindzen (1981), the representation of flow blocking calls for specific diagnostics and drag formulations (Lott & Miller, 1997). All these effects are now taken into account in most weather prediction and climate models (Hájková & Šácha, 2024; Kim & Doyle, 2005; Scinocca & McFarlane, 2000; Vosper, 2015), and their parametrization continues to be improved (van Niekerk & Vosper, 2021). They are often called subgrid-scale orography (SSO) parametrizations, which is somewhat misleading because TOFD is also a subgrid-scale parametrization. According to Beljaars *et al.* (2004), SSO parametrization should concern mountains with horizontal scale $L > 5000\,\mathrm{m}$, but remains fully active even in the most recent models that have horizontal resolutions that approach this scale (Giorgetta *et al.*, 2018; Pithan *et al.*, 2016; Sandu *et al.*, 2015). In fact, it is not so clear whether there is a critical mountain size ($L < 5000\,\mathrm{m}$) below which the mountain would only impact the boundary layer and above which the mountain would only impact the waves. We actually believe that this criterion is quite ad hoc and should depend on the nature of the flow. We also know that the effective resolution of a model largely exceeds the grid scale (Skamarock, 2004; Vosper *et al.*, 2016), which means that SSO parametrizations will probably remain necessary in the foreseeable future and at scales for which TOFD and SSO parametrizations cannot be separated.

Because we know that boundary-layer dynamics are highly controlled by the inviscid solutions aloft, and because in mountain meteorology the wave forcing is embedded in the boundary layer, it soon appeared that the two communities should make some effort to integrate results from the other community. It is in this context that Hunt *et al.* (1988a), Belcher and Wood (1996), and Weng *et al.* (1997) included stratification and gravity waves in boundary-layer theories over mountains. Belcher and Wood (1996) showed that when the Froude number $F = U/NL$ is smaller than 1, the mountain drag was due to mountain gravity waves (rather than boundary-layer effects) and was well predicted by linear mountain gravity wave theory. This result actually depends on the height at which one chooses the reference velocity U and reference Brunt–Väisälä frequency N. A comparable analysis has been made recently by Lott *et al.* (2024), using a formalism where the gravity wave dynamics is much more complete than in Belcher and Wood (1996), in the sense that it explicitly includes trapped waves and evaluates uniform approximations that can be used to evaluate the vertical profiles of the wave Reynolds stress. As TOFD and SSO parametrizations root in linear theories, and as the neutral results in Lott *et al.* (2024) reproduce the non-separated sheltering parametrized in TOFD and the stratified results the trapped and propagating waves parametrized in SSO, it could provide insight on how to combine these two parametrizations. Of course, linear analysis is not complete when it comes to predict nonlinear processes like flow separation, blocked flow drag, and separated sheltering. In this sense, our work is a quite conceptual unification, but we can follow Lott and Miller (1997) and use linear theory to predict the altitude at which separation is likely to occur. The linear analysis is also incomplete to represent wave breaking and hydraulic jumps, but for these we more or less assume that conventional approaches following Lindzen (1981) remain appropriate to predict breaking (with hydraulic jumps occurring when breaking occurs at low level). Linear theory also has the advantage that the problem can be solved in Fourier space wave number by wave number without interaction between the wave numbers. With the resulting solutions for fluxes of momentum, we can integrate over a realistic orographic source spectrum to find the relevant fluxes. This is already applied in TOFD, but

most SSO schemes still represent subgrid orography using a simple characterization by standard deviation of amplitude and slope (i.e., by typical subgrid mountain height and distance between ridges).

The main results in Lott *et al.* (2024) are that the dynamics is controlled by two vertical scales. For a disturbance with horizontal wave number k the first is the inner layer scale $h_i(k)$ defined by

$$kU(h_i(k)) \approx \frac{\nu'}{h_i^2}, \tag{1}$$

where $U(z)$ is the background wind profile and ν' the turbulent diffusion coefficient acting on the disturbance. It characterizes the depth of the "inner" layer over which turbulent diffusion impacts the disturbance dynamics, in contrast with the "outer" layer where the disturbance dynamics is inviscid. The second is the altitude of the turning level $h_t(k)$, where the Scorer parameter equals wave number squared:

$$S(h_t(k)) = \frac{N^2}{U^2} - \frac{U_{zz}}{U} = k^2. \tag{2}$$

$h_t(k)$ is the height beyond which upward-propagating waves cannot propagate any more and are reflected. Lott *et al.* (2024) consider cases where reflections mainly occurs in the "outer" layer (i.e., for $h_t(k) > h_i(k)$) and are within an externally imposed "boundary layer" of characteristic depth d. More precisely, the disturbances that are "trapped" have $h_i(k) < h_t(k) < d$ quite systematically, and the "freely propagating" disturbances that do not encounter turning levels are referred to disturbances with $h_t(k) = \infty$.

Lott *et al.* (2024) also conclude that $h_i(k)$ controls the amplitude of the forcing, whereas $h_t(k)$ controls the nature of the dynamics. More specifically, the intensity of the incident wind and stratification that produces disturbances when the flow interacts with the hill has to be measured at the inner-layer height ($U(h_i)$ and $N(h_i)$). The reason is that the flow is pushed over a surface disturbance and a viscous layer up to height h_i. This flow displacement is slightly out of phase with the surface undulation and results in drag, even in the neutral case. In the literature (e.g., Belcher & Hunt, 1998) it is known as drag due to non-separated sheltering. For the nature of the dynamics, the flow response is neutral when most of the turning levels are close to the surface compared with the mountain length L, stratified when they are far away, and intermediate in situations being associated with trapped lee waves. Note that the stratified cases include situations without turning levels ($h_t(k) = \infty$ for most k).

Although we argue that linear theory could help to combine parametrizations of turbulent orographic form drag and subgrid-scale orography, the fact that the second includes upstream separation and blocking effects that are not explicitly included in the first remains a difficulty. To incorporate such effects in more neutral cases, we need a criterion that can potentially include downstream separation and sheltering effects. For this purpose, we propose to include non-hydrostatic effects in the blocking criterion and consider that the linear theory should only take into account the flow above the blocking altitude.

This article is structured as followings. Section 2 provides a summary of the theory (Lott *et al.*, 2024), the choices made with respect to the background flow properties (unperturbed wind and temperature profiles), and a definition of the relevant dimensionless parameters (Froude number and Richardson number). Section 3 describes results of the linear model classified according to Froude and Richardson numbers, which clearly separates propagating wave, trapped wave, and neutral drag regimes. It automatically leads to a physically based scheme for low-level drag and how it is distributed in the vertical. Section 3 also discusses briefly how criteria for flow blocking can be extended to included sheltering. Section 4 summarizes and discusses how our results could be used to upgrade state-of-the art TOFD and SSO parametrizations. It also discusses remaining issues that need further work.

2 | THEORY, BACKGROUND FLOW PROPERTIES, AND DIMENSIONLESS PARAMETERS

Our analysis is based on the linear response to a mountain forcing in the two-dimensional (2D) linear Boussinesq equation, using terrain-following coordinates X, Z (Lott *et al.*, 2024):

$$x = X, \quad z = Z + h(X)f(Z), \tag{3}$$

where $h(X)$ is the mountain height and x and z are the horizontal and vertical Cartesian coordinates respectively. The function $f(Z)$ ensures the transition from terrain-following coordinates near the surface to Cartesian coordinates by taking $f(0) = 1$ and decaying towards zero for $Z \to \infty$. The model variables are u (horizontal wind), w (vertical velocity), $\boldsymbol{w} = u(\partial Z/\partial x) + w(\partial Z/\partial z)$ (velocity perpendicular to $Z =$ cte surfaces), p (pressure), and b (buoyancy, defined as $g\theta/\theta_r$ with g for gravity, θ for potential temperature and θ_r a constant reference value). Model variables are expanded in a background in capital letters and perturbations primed; that is, $u = U + u'$, $p = P + p'$, and $b = B + b'$. w and $\boldsymbol{w}$ are perturbations only; that is, $w = w'$ and $\boldsymbol{w} = \boldsymbol{w}'$.

Following Clark (1977) and assuming small perturbations, a set of linear stationary Boussinesq equations

can be derived. They contain a turbulent viscosity, and given the linearity they can be most conveniently solved in wave-number space—see Lott *et al.* (2024) for details and the Appendix for the equations. For simplicity, mixing-length closure is used without considering stability effects in a standard boundary-layer approximation that neglects horizontal turbulent fluxes. The vertical fluxes of momentum and buoyancy are

$$\tau = \nu \frac{\partial u}{\partial Z} \quad \text{and} \quad q = \nu \frac{\partial b}{\partial Z}, \quad \text{with} \quad \nu = l^2 \left\| \frac{\partial u}{\partial Z} \right\|, \tag{4}$$

where l is the mixing length and $\kappa = 0.4$ the von Kármán constant. To simplify the theory in the outer layer, Lott *et al.* (2024) take

$$l = l_\infty \tanh\left(\kappa \frac{Z + z_0}{l_\infty} \right) \tag{5}$$

rather than the Blackadar (1962) expression valid for neutral flows. It keeps $l \approx \kappa Z$ near the surface and $l \approx l_\infty$ in the far field but avoids a significant log dependence of the background winds in the far field. With this expression, the horizontal wind and buoyancy profiles that give uniform fluxes are

$$\begin{aligned} U_V(Z) &= \frac{u_*}{\kappa} \log\left[\frac{\sinh \kappa (Z + z_0)/l_\infty}{\sinh \kappa z_0 / l_\infty} \right], \\ B_V(Z) &= \frac{b_*}{\kappa} \log\left[\frac{\sinh \kappa (Z + z_0)/l_\infty}{\sinh \kappa z_0 / l_\infty} \right], \end{aligned} \tag{6}$$

with u_* and b_* being the friction velocity and buoyancy scale respectively. The Brunt–Väisälä frequency is given by

$$\begin{aligned} N^2(Z) = \frac{dB_v}{dz} &= N(\infty) \left\{ \tanh\left[\frac{\kappa (Z + z_0)}{l_\infty} \right] \right\}^{-1}, \\ \text{where } N(\infty) &= \frac{b_*}{l_\infty}. \end{aligned} \tag{7}$$

As in Equation (6) $U_V(\infty) = \infty$, gravity waves cannot propagate in the far field, so the background velocity is modified to become

$$U(Z) = U(\infty) \tanh\left(\frac{l_\infty}{u_* d} U_V(Z) \right), \text{ where } U(\infty) = \frac{u_* d}{l_\infty}. \tag{8}$$

This introduces a boundary-layer depth d around and above which the background flow is externally imposed rather than being an exact solution of the viscous equations. In this case the background flow can evolve in time; it occurs at a time-scale around $T = (U(\infty)d)/u_*^2$, which is much longer than the advective time-scale $T_a = U(\infty)/L$, where L is the mountain horizontal length (i.e., $T/T_a \approx\approx d^3/(Ll_\infty^2) \gg 1$).

In Lott *et al.* (2024), disturbance equations are solved for Gaussian mountains:

$$h(x) = H\, \mathrm{e}^{-x^2/2L^2}, \tag{9}$$

with H the mountain height. The far-field profile characteristics and the horizontal mountain scale define a Froude number F that turns out to be highly relevant for the flow regime, as will be shown later:

$$F = \frac{U(\infty)}{N(\infty)L} = \frac{d}{L\sqrt{J}}. \tag{10}$$

Here, J is a Richardson number measured in the boundary layer above the surface layer:

$$J = \frac{l_\infty b_*}{u_*^2} \approx \frac{N^2}{(\partial U/\partial z)^2} (l_\infty \ll z \ll d). \tag{11}$$

For fixed F, it will be used to distinguish "neutral" and "stratified situations".

Examples of vertical profiles of $N(Z)$ and $U(Z)$, according to Equation (7) and Equation (8) respectively, are shown in Figure 1a,b, respectively. In them, we choose quite strong values for the friction velocity, roughness length, and limit value of the mixing length, which explicitly assumes that we consider rough terrain. The Brunt–Väisälä frequency in Figure 1 decreases uniformly with altitude, as expected when colder surfaces impose stratification, but stays quite small when $b_* = 1.5 \times 10^{-4}\ \mathrm{m} \cdot s^{-2}$ (red in Figure 1a). In this case, its minimal value in the far field is $N(\infty) \approx 4 \times 10^{-3}\ \mathrm{s}^{-1}$, which we will consider as almost neutral flow. For larger b_* (green in Figure 1a), the Brunt–Väisälä frequency $N(\infty) \approx 1.253 \times 10^{-2}\ \mathrm{s}^{-1}$, which is quite common for the free atmosphere in a stable winter configuration. The background wind in Figure 1b is shown for the same two values of the turbulent buoyancy scale with two different values of the Froude number. In this article we make the choice to keep the boundary-layer characteristics u_*, b_*, l_∞, and z_0 constant and only change b_* to distinguish neutral and stratified situations. The horizontal scale of the mountain L is set to 1 km. These choices make depth d dependent on the Froude number F and Richardson number J (or b_*); see Equation (10). For neutral configurations and small Froude number ($J = 0.1, F = 0.5$), this results in a d that is quite small, the boundary layer stays confined near the surface, and the background wind is small at all altitudes with typically $U < 2\ \mathrm{m} \cdot \mathrm{s}^{-1}$. We will present results for this case for completeness but will mostly detail the other configurations which look more reasonable. In them the incident wind varies from moderately strong in the far field to very strong when d/L changes from $d/L = 0.5$ to $d/L = 4$.

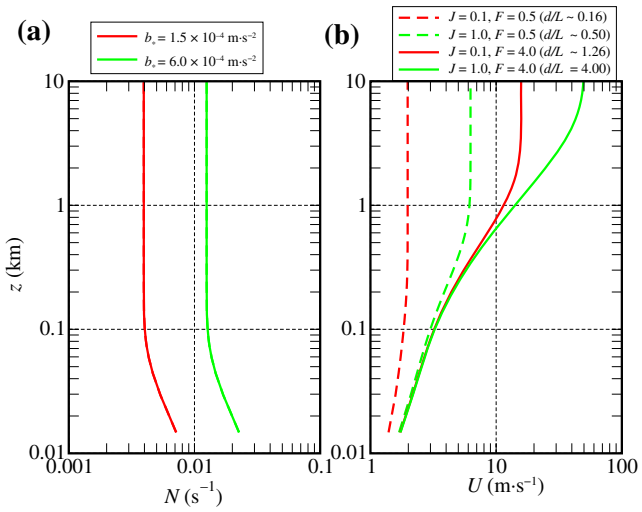

FIGURE 1 Background profiles of (a) Brunt–Väisälä frequency and (b) wind for two turbulent buoyancy scales b_* and two Froude numbers F. All the other parameters are fixed: $u_* = 0.25$ m · s^{-1}, $l_\infty = 20$ m, $z_0 = 1$ m, and $L = 1$ km. Boundary-layer depth d is controlled by Equation (10). [Colour figure can be viewed at wileyonlinelibrary.com]

When slope $S = H/L \ll 1$ and the limit value of the mixing length $l_\infty \ll L$, Lott *et al.* (2024) search disturbances to the background winds in the form of Fourier transforms:

$$w'(X,Z) = \int_{-\infty}^{+\infty} \widehat{w}(k,Z)\, \mathrm{e}^{\mathrm{i}kX}\, dk, \tag{12}$$

with similar expression for b', p', u', and $\boldsymbol{w}'$, the disturbances of, respectively, buoyancy, pressure, horizontal velocity, and velocity perpendicular to the $Z =$ cte surfaces. The disturbance equations considered in Lott *et al.* (2024) are written in dimensional form in the Appendix, they are solved using matched asymptotics between the outer and inner layers, which permits the imposition of no-slip boundary conditions in $Z = 0$ ($\widehat{u} = \widehat{w} = \widehat{b} = 0$) and radiation condition in $Z \to \infty$; that is,

$$\widehat{w}(k, Z \approx \infty) = A(k)\, \mathrm{e}^{\mathrm{i}(k_c^2 - k^2)^{1/2} Z}, \tag{13}$$

where the "cut-off" wave number $k_c = 1/(FL)$ and $k > 0$ to ensure upward propagation and with the convention $\sqrt{-1} = \mathrm{i}$ to ensure evanescent waves when there are turning levels (when $k > k_c = 1/(FL)$). The solution for $k < 0$ is obtained by complex conjugation and the amplitude of each harmonics $A(k)$ deduced from the surface boundary conditions after integration of Equations (A.1a–A.1e).

To anticipate the response to the mountain forcing, Figure 2 shows the mountain forcing $\widehat{h}(k)$ in spectral space, the turning levels, and the inner levels as a function of horizontal wave number. The altitudes of the turning levels are visualized by displaying $\sqrt{S(z)}$ on the k-axis, and the turning levels by inverting numerically Equation (1) using $\nu' = 2lu_*$—see the diffusion coefficient in Equation (A.1a):

$$k\, U(h_i(k)) = \frac{2lu_*}{h_i(k)^2}. \tag{14}$$

The first thing to notice is that the inner levels depend little on the J and F parameters. There are four almost indistinguishable blue dotted curves, and they are generally located at substantially lower altitude than the turning levels. This means that in all cases and for most harmonics there is a large space between the inner layer and the turning levels where the dynamics is predominantly inviscid. The second thing to notice is that, for small Froude number ($Fr = 0.5$, dashed lines), most of the harmonics forced by the mountain are not trapped; that is, $k < k_c$ for most k where the power spectrum of h is large. This is in contrast to the cases at larger Froude number ($F = 4$, solid lines), where most of the harmonics are trapped; that is, $k > k_c$ for most harmonics forced by h. Furthermore, for the larger F, if we contrast cases between neutral and stratified, one sees that more of the trapped waves have turning levels located nearer the surface in the neutral case (solid red line) than in the stratified case (solid green line). According to Lott *et al.* (2024), the latter potentially favours the development of trapped lee waves provided that the turning level altitudes are larger than or comparable to the horizontal scale of the disturbances. To substantiate the comparison harmonic by harmonic, the black dotted curve shows their horizontal scale $1/k$. In the stable case ($J = 1$ in solid green), $h_t(k) \approx 1/k$ and becomes even larger when $k < 0.4\,\mathrm{km}^{-1}$. The turning levels are now sufficiently elevated compared with the horizontal scales for trapped waves to develop. On the contrary, in the neutral case ($J = 0.1$, solid red), $h_t(k) \ll 1/k$, except of course when the harmonics are no longer trapped (i.e., when $k < k_c$).

3 | LINEAR RESULTS

3.1 | Vertical velocity field

We plot in Figure 3 the vertical velocity field w' when the flow has parameters as in Figure 1. The first interesting thing to notice is that, in all panels, w' has characteristic amplitudes around 50 cm · s^{-1} that scale as $U(h_i)H/L$: according to Figures 2 and 1 h_i and $U(h_i)$ have characteristic values of around 100 m and 1–5 m · s^{-1} respectively. This is the amplitude of the vertical velocity produced when an inviscid flow of speed $U(h_i)$ passes over a ridge

of slope H/L. The interpretation given by Lott *et al.* (2024) is that below h_i dissipative effects force streamlines to be displaced in the vertical following the mountain, and above that inviscid dynamics takes over. This result will be central in our estimations of the drag and stresses. If we now analyse the differences, we see that for small Froude number (Figure 3a,c) the response is dominated by upward-propagating waves with almost no trapped waves in the neutral case (Figure 3a) and quite a weak low-level signal in the stratified case (Figure 3c). In the latter, note, nevertheless, that at low level the vertical velocity presents oscillations with wavelength $\lambda = 2\pi/k \approx 3$ km, which is near the "cut-off" wavelength $2\pi/k_c$. This predominance of trapped oscillations near the cut-off wavelength is discussed in detail by Pauget *et al.* (2024). The results at larger Froude number in Figure 3b,d show much less upward-propagating waves, consistent with the fact that most harmonics encounter turning levels. There is, nevertheless, a strong contrast between the neutral and stratified configuration: trapped modes are almost absent in the neutral case (Figure 3b), whereas a quasi-resonant mode dominates in the stratified case (Figure 3d). Its horizontal wavelength is around $2\pi/\lambda \approx 15$ km, which is significantly smaller than the "cut-off wavelength" $2\pi/k_c \approx 25$ km. Basically, when stratification increases from neutral to stratified the turning levels' altitudes increase, the higher turning levels being for wave numbers larger but near the cut-off value k_c (see Figure 2). When the turning levels are sufficiently high compared with the characteristic scale of the mountain, the trapped modes start to propagate downstream. It occurs first near the cut-off wave number (as in Figure 3c), eventually moving to higher wave number when the turning levels become higher (as in Figure 3d).

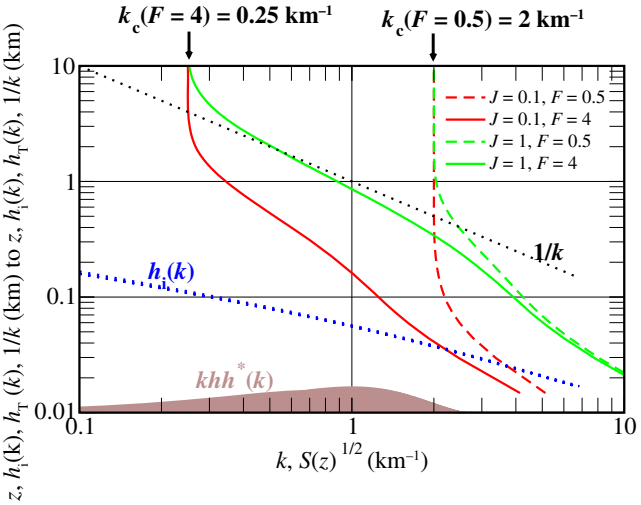

FIGURE 2 Mountain power spectrum multiplied by k for the Gaussian hill with $L = 1$ km (brown) and turning levels (red and green) as a function of horizontal wave number for the same parameters as in Figure 1. The dotted curves are the inner layer depth $h_i(k)$ (blue) and horizontal scale $1/k$ (black). [Colour figure can be viewed at wileyonlinelibrary.com]

3.2 | Pressure drag and wave Reynolds stress

To estimate the contribution of each harmonic to drag and stress, we compute the momentum flux (MF) in terrain-following coordinates along $Z =$ cte surfaces:

$$\hat{D}(k, Z) = \Re\{-\rho_r \hat{u}\hat{w}^* + ikf(Z)\hat{h}\hat{p}^*\}. \quad (15)$$

The asterisk indicates complex conjugate, $\Re$ is the real part, and the function $f(Z)$ is from the curved coordinate definition, Equation (3). At $Z = 0$, for instance, $f(0) = 1$ and Equation (15) is the mountain drag, since $\hat{w} = 0$; for

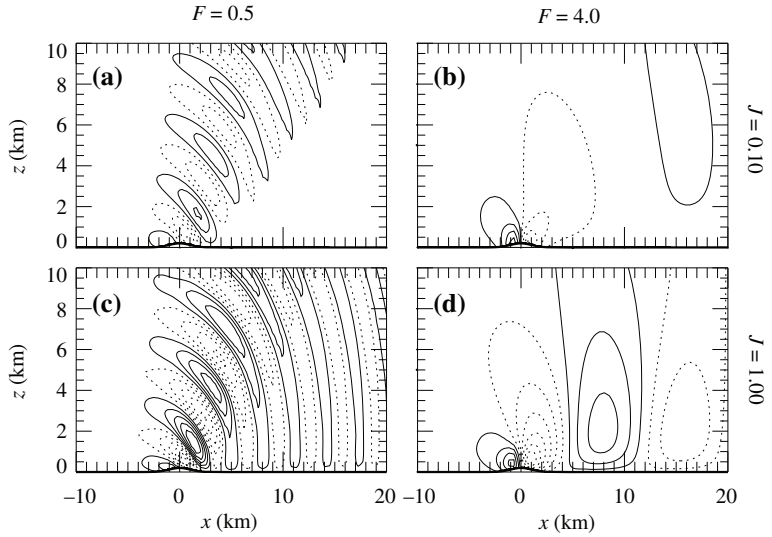

FIGURE 3 Vertical velocity field for various values of J and F, in all simulations $u_* = 0.25$ m · s^{-1}, $\lambda = 20$ m, $z_0 = 1$ m, $L = 1$ km, and the mountain height $H = 200$ m. To keep F unchanged when J varies, the boundary-layer depth $d = \sqrt{J}FL$. In all panels, the contour interval is 10 cm · s^{-1}.

$z \to \infty$, however, the Z-surfaces are horizontal, $f(Z) = 0$, and the formula gives the conventional Reynolds stress, since $\widehat{\boldsymbol{w}} = \widehat{w}$. Note that Equation (15) is the representation in spectral space of the leading order of eq. (32) in Lott *et al.* (2024).

The black and red solid lines in Figure 4 show the contributions of each harmonic to the surface drag and to the gravity-wave stress in the far field, $\widehat{D}(k, 0)$ and $\widehat{D}(k, \infty)$ respectively. When the Froude number is small in Figure 4a,c, one sees that the Reynolds stress and mountain drag almost coincide. They are both substantial when the harmonics propagate upward in the far field (when $k < k_c$), and they are both small where the harmonics are evanescent in the far field. Nevertheless, when $k < k_c$, one sees that the Reynolds stress is smaller than the surface drag, because there is a small erosion of the upward waves in the inner layer. Interestingly, there is a marked difference between the neutral and stratified cases near the cut-off wave number, with the trapped mode appearing near the cut-off wave number as a narrow peak in the surface drag (see Figure 4c). The cases with more evanescent modes in Figure 4b,d are dynamically much richer. In them, one sees that in the propagating harmonics range ($k < k_c$) the drag and wave Reynolds stress almost coincide, whereas in the evanescent harmonics range ($k > k_c$) the drag can be large whereas the Reynolds stress is almost zero. More specifically, the large drag when $F = 4$ and $J = 0.1$ in Figure 4b is not likely due to trapped waves, as the signal on vertical velocity downstream of the mountain in Figure 3b is very small. It is a case where evanescent harmonics essentially contribute via a turbulent orographic form drag. On the contrary, when $J = 1$ and still for $F = 4$, Figure 4d shows a substantial peak in drag at $k \approx 0.4$, which corresponds to the horizontal wavelength of the quasi-resonant trapped wave that dominates the response in Figure 3d.

3.3 | Mountain drag and gravity-wave stress predictors

Based on the facts that (a) the vertical velocity field scales in amplitude as if the background flow incident on the mountain should be taken at the inner altitude, and that (b) at the inner layer altitude the Scorer parameter $S(h_i(k)) \gg k^2$ (see Figure 2) we propose as a first predictor of the wave drag its hydrostatic value:

$$\mathbf{D}_W(k) = \rho_r C_W k \widehat{h}\widehat{h}^* U(h_i(k)) N(h_i(k)), \tag{16}$$

where the constant C_W is a tunable parameter and $\mathbf{D}_W(k)$ is real. The physical interpretation is that the strong turbulent diffusion in the lower part of the inner layer forces the streamlines to follow the hills, and the distorted streamlines become the "effective" orography that produces the waves (see Lott *et al.*, 2020).

We also consider that turbulent form drag is the result of the pressure loss across the hill that balances changes in disturbance shear stress. To estimate it we consider that the amplitude of the horizontal wind disturbance at h_i is $\approx \widehat{h}\partial U/\partial Z(h_i)$, an estimate based on the particular solution of the problem in curved coordinates; see Lott *et al.* (2024, eq. A24). Taking into account the definition of $h_i(k)$ in Equation (14) and comparing the horizontal pressure gradient with the shear stress vertical derivative (see right-hand side in Equations A.1a–A.1e) yields $ik\widehat{p}^* \approx U(h_i)\partial U/\partial Z(h_i)\widehat{h}$. Multiplying by $\widehat{h}^*$ gives an estimate of the turbulent form drag:

$$\mathbf{D}_T(k) = \rho_r C_T k \widehat{h}\widehat{h}^* U(h_i(k)) \frac{\partial U(h_i(k))}{\partial Z}, \tag{17}$$

C_T being a second tunable parameter. This is an interesting formula since, compared with Equation (16), the Brunt–Väisälä frequency $N(h_i)$ is simply replaced by the

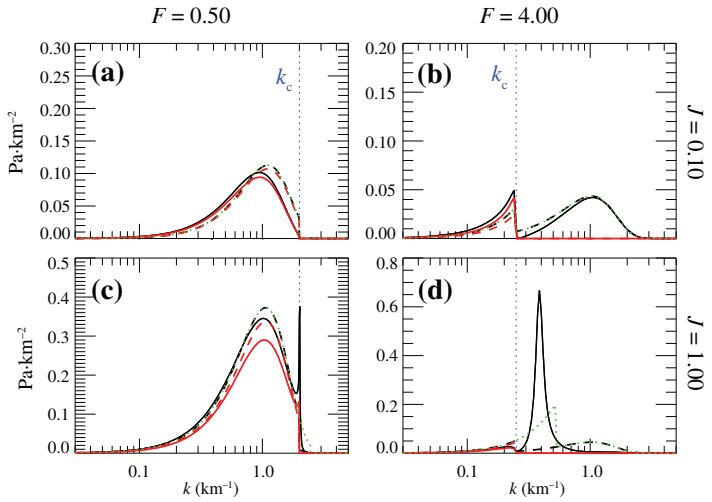

FIGURE 4 Surface drag (black solid line) and wave Reynolds stress (red solid line) as a function of horizontal wave number. The curves represent $k\widehat{D}$ rather than $\widehat{D}$, expressed in Pa · km^{-2} to preserve integration along the log-scale used for the k-axis. The dashed red curve is for gravity-wave predictor Equation (16) with $C_W = 0.4$, and the black dashed curve also includes the form drag predictor according to Equation (18) with $C_T = 0.1$. Additionally, the green dotted line includes evanescent modes according to Equation (19) with $S_t = 1$. [Colour figure can be viewed at wileyonlinelibrary.com]

wind shear $\partial U/\partial Z(h_i)$. In the following we choose eye-fit values of C_W and C_T after a few trials.

The dashed red curve in Figure 4 applies the gravity-wave stress predictor for harmonics with $k < k_c$ and taking $C_W = 0.4$. We see that it matches well the gravity-wave stress from the model for all values of F and J. For the surface pressure drag we augment gravity-wave predictor Equation (16) with turbulent form drag predictor Equation (17), taking $C_T = 0.1$, resulting in surface drag

$$\mathbf{D}_S(k) = \mathbf{D}_T(k) + \Theta(k_c - k)\mathbf{D}_W(k), \tag{18}$$

with Θ being the Heaviside function to keep gravity-wave drag for $k < k_c$ only. For small Froude number, the black dashed lines show that the inclusion of the turbulent form drag does not change the prediction much. It slightly increases the drag compared with the gravity-wave stress predictor, staying quite close to the model drag. Of course, neither of these two formulae capture the peaks in drag near k_c (Figure 4c). At large Froude number, the results are more contrasted between the neutral and stratified cases (Figure 4b,d). In both, our predictors stay valid where there are freely propagating disturbances ($k < k_c$), and the drag predictor seems to work quite well in the neutral case for $k > k_c$ (see Figure 4b); that is, when the trapped wave signal is small. However, the predictor rather fails in the stable case, when large-amplitude trapped waves control the flow at low level (see Figure 4d). Unfortunately, there is no simple way to capture the drag due to these quasi-resonant dissipative modes. The only analytical results we have stay limited to inviscid and simplified background configurations (Teixeira *et al.*, 2013a, 2013b). To circumvent that difficulty, we return to the fact that when the turning levels are sufficiently high the hydrostatic wave theory is still suitable for the prediction of drag (Lott, 1998) but overstate it when the turning levels are close to the surface. These are inviscid results, but here we have seen that trapped lee waves can develop when the turning levels' altitudes are larger than the horizontal scale of the mountain. For a single harmonic, we can translate this criterion by saying that a harmonic can contribute to the drag when $h_t(k) > 1/k$. For this reason, we next propose to extend the wave drag predictor to the evanescent modes satisfying this criterion and write

$$\mathbf{D}_S(k) = \mathbf{D}_T(k) + \Theta(kh_t(k) - S_t)\mathbf{D}_W(k), \tag{19}$$

where S_t is a tunable parameter. Note that all the propagating harmonics are included in Equation (19) since $h_t(k) = \infty$ when $k < k_c$. In Figure 4d, we take $S_t = 1$ and see on the green dotted curve that this extension of the gravity-wave drag to the evanescent sector permits one to capture a fraction of the peak in drag that is due to trapped waves. In the other panels, this extension does not play a role simply because the h_t values are too close to the surface when not infinite. We have tested our formula with many different flow configurations, varying λ, z_0, J, and F quite systematically. When we change λ and z_0 for instance, we found comparable behaviour as in Lott *et al.* (2024); namely, that predictors comparable to ours here stay qualitatively valid. This means that matches can be obtained for slightly different tuning parameters C_W and C_T. What is important here are the concepts. However, to illustrate the difficulties, Figure 5 shows the drag stresses and predictors integrated over all wave numbers,

$$D(Z) = 2\pi \int_{-\infty}^{+\infty} \mathbf{D}(k, Z)\, dk \tag{20}$$

and varying systematically the Froude number. In them one sees that it is the wave stress that is the most accurately predicted, with some overestimation in the neutral case at small Froude number. This impacts the surface drag predictor in the same range. At Froude number $F > 1$, the wave stress is well predicted in both neutral and stratified cases. The difference between the surface drag and the gravity-wave stress is important at large Froude number in both the neutral and stratified cases. In the neutral case, the TOFD predictor captures well the difference, as indicated by the dashed line in Figure 5a. In the stratified case, the TOFD predictor increases the wave drag, but not sufficiently; it is the inclusion of trapped waves that makes up the difference (see the green dotted line in Figure 5b). Clearly, at large Froude number, the predictor starts to diverge from the model, underestimating the trapped waves contribution. We found such underestimations quite common, but better predictors of the trapped waves are hard to find. Again, we have tested our predictors in Figure 5, leaving the parameters C_W, C_T, and S_t unchanged but for a much larger number of parameters. For almost all values of stability in the range $0.05 < J < 2$ and of the limit value of the mixing length in the range $10\ \text{m} < l_\infty < 40\ \text{m}$, comparable behaviour was found in the range $0.5 < F < 8$ (not shown).

As our linear dissipative theory attributes the differences between surface drag and wave stress to three different causes—inner layer erosion of propagating modes, inner layer erosion of evanescent modes, or dissipated trapped lee waves—we can ask ourselves if the drag at low level will be distributed differently in the vertical. For this purpose, Figure 6 shows vertical profiles of the MFs $\mathbf{D}(k, Z)$ for different wave numbers, where for each wave number the altitude has been normalized by the inner layer altitude. When there are almost no evanescent modes in the neutral case (Figure 6a) the MFs are almost uniform, although some erosion occurs below $z < 3h_i(k)$

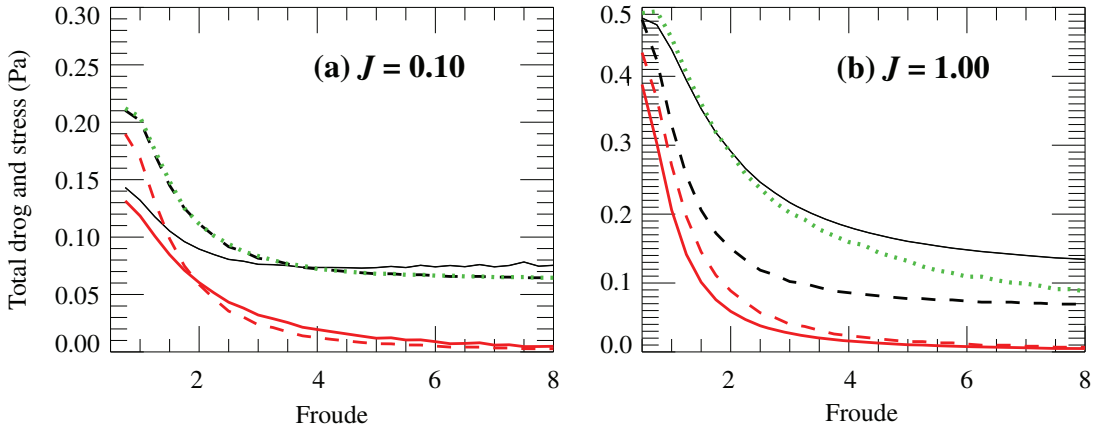

FIGURE 5 Drag integrated over wave number for the Gaussian hill, as a function of the Froude number with (a) $J = 0.1$ and (b) $J = 1$. The solid black curve is for surface drag and the solid red curve for gravity-wave stress, both from the linear model. The dashed black curve represents the turbulent orographic form drag (TOFD) predictor, the dashed red the gravity-wave stress predictor, and the dotted green curve includes TOFD + gravity wave + trapped waves predictors according to Equation (19). [Colour figure can be viewed at wileyonlinelibrary.com]

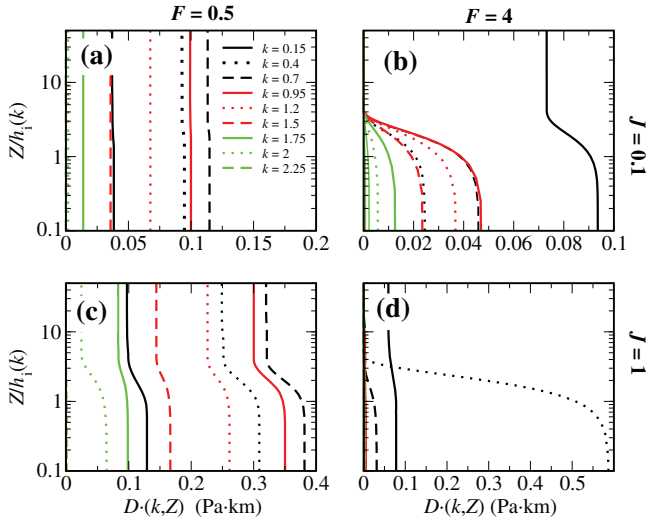

FIGURE 6 Vertical profiles of momentum fluxes $\hat{D}(k, Z)$ for a range of wave numbers (see legend, with k in km^{-1}). [Colour figure can be viewed at wileyonlinelibrary.com]

to $z \approx 4h_i(k)$ in the stable case (Figure 6c). Compared with Figure 6a, there is some erosion of the MFs because the gravity waves have a shorter vertical wavelength and are hence more affected by dissipation (see Pauget *et al.*, 2024). At large Froude numbers, most of the evanescent harmonics that contribute to the drag see their MFs decreasing between the surface and $z < 3h_i(k)$ to $z < 4h_i(k)$ again. This is the same vertical distance over which the propagating harmonics are affected. Whatever the dynamics, from the many dissipated evanescent harmonics seen in Figure 6b, to the trapped mode that strongly contributes in Figure 6d, the MFs always decrease over the same distance, which is about $3h_i(k)$ to $4h_i(k)$. Of course, this is not a surprise; all modes being steady, we know from Eliassen and Palm (1962) that the MFs can only decay where there is dissipation, which occurs here over distances scaled by h_i.

3.4 | Predicting blocking/sheltering depth

The fundamental concept used to predict flow blocking in Lott and Miller (1997) is that, according to Smith (1980), linear theory can be used to predict the blocking altitude. More specifically, Lott and Miller (1997) tells at which altitude an air parcel, initially located at an altitude z_b and forced to move up, will no longer ascend vertically when reaching the mountain top. In the full three-dimensional case, the air below z_b eventually contours the obstacle, whereas in the 2D case a cavity of stagnant air can form and piles up on the upstream side—an example of 2D non-separated blocking can be found in Lott *et al.* (2020, fig. 7c). Whatever the geometry and consequences of the blocking we can use a Wentzel–Kramers–Brillouin approach in all cases to calculate the phase change between z_b and the mountain top H and the test when it exceeds a non-dimensional threshold H_{NC}

$$\int_{z_b}^{H} \frac{N}{U}\, dz = H_{NC}. \tag{21}$$

Here, we have used the hydrostatic approximation to express a local vertical wave number. We could alternatively get closer to the approach of Smith (1980) and search when the horizontal velocity produced by the wave forced by a hill of height $H - z_b$ balances the incident wind at that height (times the non-dimensional threshold

H_{NC}). Still, in the hydrostatic case, this gives

$$u' \approx N(z_b)(H - z_b) \approx U(z_b) * H_{NC}, \tag{22}$$

the last two terms yielding a criterion quite comparable to Equation (21). An advantage of using Equation (22) is that it can easily be extended to the non-hydrostatic case. If we use linear Wentzel–Kramers–Brillouin theory to calculate u' produced by $h(x) - z_b$ we have

$$u' = U(z_b)\int_{-\infty}^{+\infty} -\mathrm{i}\ \mathrm{sign}(k)\sqrt{\frac{N^2}{U^2} - k^2}(\hat{h} - \hat{z}_b)\ dk. \tag{23}$$

We can simplify further and consider that the Fourier transform of the hill above the blocked flow stays near the Fourier transform of the hill: $\hat{h} - \hat{z}_b = (H - z_b)\hat{h}/H$, in which case the condition $|u'| \approx H_{NC}U$ can be written

$$\frac{H - z_b}{H}\int_{-\infty}^{+\infty}\sqrt{\left|\frac{N(z_b)^2}{U(z_b)^2} - k^2\right|}\hat{h}(k)\ dk \approx H_{NC}. \tag{24}$$

In the case of uniform flow and a Gaussian ridge,

$$\mathbf{h} = \frac{LH}{\sqrt{2\pi}}\ \mathrm{e}^{(-k^2L^2)/2},$$

this condition reduces to

$$\frac{(H - z_b)N(z_b)}{U(z_b)} = H_{NC} \text{ and } \frac{2}{\sqrt{\pi}}\frac{H - z_b}{L} = H_{NC} \tag{25}$$

in the hydrostatic stratified case and in the non-hydrostatic neutral case respectively. We recognize the criteria for the non-dimensional height used in stratified flow dynamics, Equation (23), and a slope criterion in the neutral case.

4 | SUMMARY AND DISCUSSION

4.1 | Upgrading TOFD and SSO

The assumption of most parametrizations of subgrid-scale mountains is that mountain flow dynamics can be described by three conceptual models whose relevance depends on a non-dimensional mountain height, $H_N = HN/|U|$ and slope $S = H/L$ parameters.

For small H_N and very small slope S, the mountain drag is due to "upward"-propagating waves, whose value is estimated via hydrostatic predictors. In our Boussinesq 2D framework this drag due to upward-propagating waves (UW) can be written as

$$D_{UW} = \overline{UN}\int_0^{\infty}\rho_r C_W k\hat{h}\hat{h}^*\ dk, \tag{26}$$

where $\overline{U}$ and $\overline{N}$ are typically averaged between the surface (or a blocked-flow altitude) and the mountain top. The fact that the incident winds and stability estimate are independent of wave number eases integration, and this assumption is made in all existing schemes, to our knowledge. In our calculation, we propose to change this into

$$D_{UW} = \int_0^{k_c} C_W\rho_r k\hat{h}\hat{h}^* U(h_i)N(h_i)\ dk, \tag{27}$$

which is quite close, at least conceptually. We take into account non-hydrostatic effects by limiting the contribution of the upward-propagating waves to those not reaching turning levels in the lower troposphere, which requires identifying k_c. Note that we do not take into account non-hydrostatic effects in the integrand, which is in contrast with Smith and Kruse (2017), and because they are not significant in our cases. The momentum deposit due to those waves can be treated using conventional breaking criteria. A difficulty in our case is that the level at which U and N are evaluated varies with wave number, which complicates the integration. Nevertheless, in terms of amplitude, the fact that we propose to take winds and stability at the inner layer altitude should not make a big difference because boundary-layer turbulence smears out disturbances typically over a depth of more than 100 m. At the current resolution of most models, these altitudes should not be too far from those of the subgrid-scale orography. Treating breaking could either be done harmonic by harmonic, or by making hypotheses on the spectral distribution of the wave-induced vertical displacement to detect overturning and limit it.

Still, at small H_N but larger S, when the incident flow is more neutral, TOFD drag needs to be applied. Following Beljaars *et al.* (2004, eq. 9), we can write

$$D_T = \int_{k_0}^{\infty}\rho_r C_T k^2\hat{h}\hat{h}^*|U(h_m)|^2\ dk,$$
$$\text{where the height } h_m = \frac{c_m}{k} \tag{28}$$

and where C_T and c_m are tunable parameters. This expression translates linear dynamics (the drag is proportional to the square of the slope), and we propose to modify this to

$$D_T = \int_0^{\infty}\rho_r C_T k\hat{h}\hat{h}^*|U(h_i)|\left|\frac{dU}{dZ}(h_i)\right|\ dk. \tag{29}$$

In our framework, the inner-layer height is the height at which background turbulence affects disturbances, and this can be quite high; for example, around 100 m for our 1-km-long ridges (see Figure 2, whereas Beljaars *et al.* (2004) take $c_m = 0.1$, which results in comparable altitudes. Concerning the vertical distribution of the drag, this

is done for each harmonic over scale $l_w = 2/k$ capped by around 500 m in Beljaars *et al.* (2004), again comparable to the decay over $3h_i$–$4h_i$ seen here in Figure 6. Note that Beljaars *et al.* (2004) then make other simplifications and integrate over wave number to fasten the parametrization and ensure its stability, which we leave for further analysis. A novelty here is that we propose to include a trapped wave drag at low level, acting on the same depth as D_T, and which is just the wave drag extended between k_c and k_t:

$$D_{TW} = \int_{k_c}^{k_t} C_W \rho_r k \widehat{h}\widehat{h}^* U(h_i) N(h_i)\, dk,$$
$$\text{where } k_t h_t(k_t) = S_t \tag{30}$$

and where S_t is another tuning parameter ($S_t = 1$ in our calculations; see (Figures 4 and 5)). The extension of the wave drag at trapped wave numbers here could provide the low-level drag needed in the stable case when the turbulent drag is not strong enough (the long-tail problem; see Tsiringakis *et al.* (2017)). There is a marked difference, nevertheless: the wave drag in Tsiringakis *et al.* (2017) is evaluated with wind and stratification taken at the boundary-layer height and is entirely redistributed over that height. There is no distinction between trapped or freely propagating waves, and the dynamics at work is more related to freely propagating waves reaching critical levels in the boundary layer Nappo and Chimonas (1992). In our case, the low-level drag is explicitly due to trapped waves. Critical levels can also occur, but only for the upward waves contributing to the drag in Equation (27), providing that we treat their propagation and breaking according to the direction of their horizontal wave number Martin and Lott (2007).

Finally, for large H_N and/or S we know that part of the flow is either blocked upstream (large H_N, small S) or downstream (the sheltering effect occurring in the neutral case; small H_N, large S). Without checking numerically, we propose to replace conventional blocked flow criteria like in Equation (21) by its non-hydrostatic extension, Equation (24). The next step could be to apply low-level drag below that level, as described in Lott and Miller (1997, eqs 4 and 5).

4.2 | Discussion and further challenges

As weather prediction and climate model resolution increases and gravity waves at least become partly resolved, it could mean that a tipping point will soon be reached in the domain of subgrid-scale orography parametrization. It may well be that gravity waves and related nonlinear processes (flow blocking) no longer need to be parametrized and that we should only consider how the unresolved subgrid-scale orography feeds turbulence. For a variety of reasons, which include that the model grid scale is not representative of the model effective resolution, it does not seem to be the case in the foreseeable future. Nevertheless, it is quite certain that models are reaching scales where the interplay between gravity waves and turbulent boundary layers should be considered. The example we provide here of a simplified boundary layer interacting with a small-slope hill is a first step in this direction. By proposing moderate changes in existing parametrizations, it illustrates how they can be combined. For example, the often assumed scale separation between TOFD and SSO parametrization needs to be made flow dependent, and we show here that it could be done by evaluating a cut-off wave number k_c obtained, for instance, by minimizing the Scorer parameter in the troposphere. We also show that wave drag and turbulent orographic form drag could have similar expressions, simply changing the buoyancy frequency N into wind shear $\partial U/\partial Z$ when neutral dynamics start to dominate. Also, trapped lee waves can be taken into account by comparing the horizontal wave number of each harmonic to their turning height altitude.

Beyond these quite reasonable results, and giving credit to the predictors we provide, numerous difficulties remain. First, our drag expressions need to be integrated over wave numbers, which is potentially involved and may necessitate numerous idealized tests using single-column models and realistic orographic spectra (Beljaars *et al.*, 2004). There is also the difficulty of accounting for turning levels; for instance, when the wind turns with altitude within the boundary layer (Martin & Lott, 2007; Shutts, 1995). Also, all our background fields and predictors involve inner-layer depths, which measure the altitude at which turbulence impacts subgrid-scale dynamics, and that can be difficult to evaluate. If it cannot be worked out from the boundary-layer scheme where a disturbance dissipates, other solutions may exist—like taking the inverse of the horizontal wave number as in Beljaars *et al.* (2004), or a mid-level altitude as in Hunt *et al.* (1988b)—but these need further study.

Although we think that this study offers improvements over existing schemes for subgrid orogaphy, we also recognize the limitations that need further work. The simplest improvement is probably the extension to three-dimensional orography, particularly if it is assumed that subgrid orography is isotropic: impact studies have shown that the significance of anisotropy is very limited (Elvidge *et al.*, 2019). More seriously, in the current study, the turbulence model is a mixing-length scheme that does not consider the influence of stability on turbulent diffusion. It also assumes a "quasi-equilibrium" usually valid when changes in the forcing are assumed to be slow compared with the time-scale that turbulence

takes to reach equilibrium. The latter is a good approximation, particularly close to the surface where the turbulence time-scales are short, but it becomes less accurate for perturbations from subgrid orography. For those cases Beljaars *et al.* (1987) have shown that more complete and higher order closures are important, particularly to simulate the stress profiles. For the surface drag, and in a review of schemes, Xu and Taylor (1995) conclude that the level of closure is more important than using a full nonlinear model. More fundamentally, if our calculations somehow take into account the impact of turbulence on waves and on the wave duct, they completely neglect the feedback of waves on the turbulence itself, and additional mixing may occur (Sun *et al.*, 2015; Vosper *et al.*, 2018). Our calculations also neglect that enhanced subgrid-scale mixing is more likely to occur on the lee side of the mountains; for instance, where trapped waves produce rotors. In this case, the trapped waves can produce vertical exchange of heat, a possibility we have completely excluded here.

ACKNOWLEDGEMENTS

We thank Hugo Bellenger and Aymeric Levy-Dauchez for their constructive feedbacks. The theoretical model used to support the findings of this study is available from the corresponding author upon request.

CONFLICT OF INTEREST STATEMENT

The authors declare no conflict of interest.

DATA AVAILABILITY STATEMENT

The data that support the findings of this study are available on request from the corresponding author. The data are not publicly available owing to privacy or ethical restrictions.

ORCID

Francois Lott https://orcid.org/0000-0003-2126-5510

REFERENCES

Ayotte, K. (2008) Computational modelling for wind energy assessment. *Journal of Wind Engineering and Industrial Aerodynamics*, 96, 1571–1590.

Belcher, S. & Hunt, J. (1998) Turbulent flow over hills and waves. *Annual Review of Fluid Mechanics*, 30, 507–538.

Belcher, S.E. & Wood, N. (1996) Form and wave drag due to stably stratified turbulent flow over low ridges. *Quarterly Journal of the Royal Meteorological Society*, 122, 863–902.

Beljaars, A., Walmsley, J. & Taylor, P. (1987) A mixed spectral finite-difference model for neutrally stratified boundary-layer flow over roughness changes and topography. *Boundary-Layer Meteorology*, 38, 273–303.

Beljaars, A.C.M., Brown, A.R. & Wood, N. (2004) A new parametrization of turbulent orographic form drag. *Quarterly Journal of the Royal Meteorological Society*, 130, 1327–1347.

Blackadar, A.K. (1962) The vertical distribution of wind and turbulent exchange in a neutral atmosphere. *Journal of Geophysical Research*, 67, 3095–3102.

Charru, F., Andreotti, B. & Claudin, P. (2012) Sand ripples and dunes. *Annual Review of Fluid Mechanics*, 45, 469–493.

Clark, T.L. (1977) A small-scale dynamic model using a terrain-following coordinate transformation. *Journal of Computational Physics*, 24, 186–215.

Durran, D.R. (1990) Mountain waves and downslope winds. *AMS Meteorological Monographs*, 23, 59–83.

Eliassen, A. & Palm, E. (1962) On the transfer of energy in stationnary mountain waves. *Geophysica Publications*, 22, 1–23.

Elvidge, A.D., Sandu, I., Wedi, N., Vosper, S.B., Zadra, A., Boussetta, S. et al. (2019) Uncertainty in the representation of orography in weather and climate models and implications for parameterized drag. *Journal of Advances in Modeling Earth Systems*, 11, 2567–2585.

Giorgetta, M.A., Brokopf, R., Crueger, T., Esch, M., Fiedler, S., Helmert, J. et al. (2018) Icon-a, the atmosphere component of the icon earth system model: I. model description. *Journal of Advances in Modeling Earth Systems*, 10, 1613–1637.

Hájková, D. & Šácha, P. (2024) Parameterized orographic gravity wave drag and dynamical effects in cmip6 models. *Climate Dynamics*, 62, 2259–2284.

Hunt, J.C.R., Leibovich, S. & Richards, K.J. (1988a) Turbulent shear flows over low hills. *Quarterly Journal of the Royal Meteorological Society*, 114, 1435–1470.

Hunt, J.C.R., Richards, K.J. & Brighton, P.W.M. (1988b) Stably stratified shear flow over low hills. *Quarterly Journal of the Royal Meteorological Society*, 114, 859–886.

Jackson, P.S. & Hunt, J.C.R. (1975) Turbulent wind flow over low hill. *Quarterly Journal of the Royal Meteorological Society*, 101, 929–955.

Kim, Y.-j. & Doyle, J.D. (2005) Extension of an orographic-drag parametrization scheme to incorporate orographic anisotropy and flow blocking. *Quarterly Journal of the Royal Meteorological Society*, 131, 1893–1921.

Lindzen, R.S. (1981) Turbulence and stress owing to gravity wave and tidal breakdown. *Journal of Geophysical Research: Oceans*, 86, 9707–9714.

Lott, F. (1998) Linear mountain drag and averaged pseudo-momentum flux profiles in the presence of trapped lee waves. *Tellus Series A, Dynamic Meteorology and Oceanography*, 50A, 12–25.

Lott, F., Beljaars, A., Pauget, L. & Deremble, B. (2024) Neutral and stratified turbulent boundary layer flow over low mountains. *Quarterly Journal of the Royal Meteorological Society*, 150, 195–212.

Lott, F., Deremble, B. & Soufflet, C. (2020) Mountain waves produced by a stratified shear flow with a boundary layer. part ii: Form drag, wave drag, and transition from downstream sheltering to upstream blocking. *Journal of the Atmospheric Sciences*, 78(4), 1101–1112.

Lott, F. & Miller, M. (1997) A new subgrid scale orographic drag parameterization; its testing in the ecmwf model. *Quarterly Journal of the Royal Meteorological Society*, 123, 101–127.

Martin, A. & Lott, F. (2007) Synoptic responses to mountain gravity waves encountering directional critical levels. *Journal of the Atmospheric Sciences*, 64, 828–848. Available from:

https://journals.ametsoc.org/view/journals/atsc/64/3/jas3873.1.xml

McFarlane, N. (1987) The effect of orographically excited gravity wave drag on the general circulation of the lower stratosphere and troposphere. *Journal of the Atmospheric Sciences*, 44, 1775–1800.

Nappo, C.J. & Chimonas, G. (1992) Wave exchange between the ground surface and a boundary-layer critical level. *Journal of the Atmospheric Sciences*, 49, 1075–1091. Available from: https://journals.ametsoc.org/view/journals/atsc/49/13/1520-0469_1992_049_1075_webtgs_2_0_co_2.xml

Palmer, T.N., Shutts, G.J. & Swinbank, R. (1986) Alleviation of systematic westerly bias in general circulation and numerical weather prediction models through an orographic gravity wave drag parametrization. *Quarterly Journal of the Royal Meteorological Society*, 112, 2056–2066.

Pauget, L., Lott, F. & Millet, C. (2024) Mountain waves developing inside and aloft stably stratified turbulent boundary layers. *Quarterly Journal of the Royal Meteorological Society*, 150, 4594–4608.

Pithan, F., Shepherd, T.G., Zappa, G. & Sandu, I. (2016) Missing orographic drag leads to climate model biases in jet streams, blocking and storm tracks. *Geophysical Research Letters*, 43, 7231–7240.

Sandu, I., Bechtold, P., Beljaars, A., Bozzo, A., Pithan, F., Shepherd, T. et al. (2015) Impacts of parameterized orographic drag on the northern hemisphere winter circulation, journal of advances in modeling earth systems. *Journal of Advances in Modeling Earth Systems*, 8, 196–211.

Schär, C. & Durran, D.R. (1997) Vortex formation and vortex shedding in continuously stratified flows past isolated topography. *Journal of the Atmospheric Sciences*, 54, 534–554.

Schär, C. & Smith, R.B. (1993) Shallow-water flow past isolated topography. part i: Vorticity production and wake formation. *Journal of Atmospheric Sciences*, 50, 1373–1400.

Scinocca, J.F. & McFarlane, N.A. (2000) The parametrization of drag induced by stratified flow over anisotropic orography. *Quarterly Journal of the Royal Meteorological Society*, 126, 2353–2393.

Shutts, G. (1995) Gravity-wave drag parametrization over complex terrain: The effect of critical-level absorption in directional wind-shear. *Quarterly Journal of the Royal Meteorological Society*, 121, 1005–1021.

Skamarock, W.C. (2004) Evaluating mesoscale nwp models using kinetic energy spectra. *Monthly Weather Review*, 132, 3019–3032.

Smith, R.B. (1980) Linear theory of stratified hydrostatic flow past an isolated mountain. *Tellus*, 32, 348–364.

Smith, R.B. & Kruse, C.G. (2017) Broad-spectrum mountain waves. *Journal of the Atmospheric Sciences*, 74, 1381–1402.

Sun, J., Nappo, C.J., Mahrt, L., Belušić, D., Grisogono, B., Stauffer, D.R. et al. (2015) Review of wave-turbulence interactions in the stable atmospheric boundary layer. *Reviews of Geophysics*, 53, 956–993.

Teixeira, M., Argaín, J. & Miranda, P. (2013) Drag produced by trapped lee waves and propagating mountain waves in a two-layer atmosphere. *Quarterly Journal of the Royal Meteorological Society*, 139, 964–981.

Tsiringakis, A., Steeneveld, G.J. & Holtslag, A.A.M. (2017) Small-scale orographic gravity wave drag in stable boundary layers and its impact on synoptic systems and near-surface meteorology. *Quarterly Journal of the Royal Meteorological Society*, 143, 1504–1516.

van Niekerk, A. & Vosper, S. (2021) Towards a more scale-aware orographic gravity wave drag parametrization: Description and initial testing. *Quarterly Journal of the Royal Meteorological Society*, 147, 3243–3262.

Vosper, S.B. (2015) Mountain waves and wakes generated by south georgia: implications for drag parametrization. *Quarterly Journal of the Royal Meteorological Society*, 141, 2813–2827.

Vosper, S.B., Brown, A.R. & Webster, S. (2016) Orographic drag on islands in the NWP mountain grey zone. *Quarterly Journal of the Royal Meteorological Society*, 142, 3128–3137.

Vosper, S.B., Ross, A.N., Renfrew, I.A., Sheridan, P., Elvidge, A.D. & Grubišić, V. (2018) Current challenges in orographic flow dynamics: Turbulent exchange due to low-level gravity-wave processes. *Atmosphere*, 9, 361.

Weng, W., Chan, L., Taylor, P. & Xu, D. (1997) Modelling stably stratified boundary-layer flow over low hills. *Quarterly Journal of the Royal Meteorological Society*, 123, 1841–1866.

Wood, N., Brown, A. & Hewer, F. (2001) Parameterizing the effects of orography on the boundary layer: an alternative to effective roughness lengths. *Quarterly Journal of the Royal Meteorological Society*, 127, 759–777.

Wood, N. & Mason, P. (1993) The pressure force induced by neutral, turbulent flow over hills. *Quarterly Journal of the Royal Meteorological Society*, 119, 1233–1267.

Xu, D. & Taylor, P.A. (1995) Boundary-layer parametrization of drag over small-scale topography. *Quarterly Journal of the Royal Meteorological Society*, 121, 433–443.

How to cite this article: Lott, F., Beljaars, A. & Deremble, B. (2026) Suggestions for unifying the parametrizations of turbulent orographic form drag, mountain wave drag, and flow blocking. *Quarterly Journal of the Royal Meteorological Society*, e70169. Available from: https://doi.org/10.1002/qj.70169

APPENDIX A

Recalling from Equation (3) that the vertical coordinate transform is written $z = Z + h(X)f(Z)$ and neglecting turbulent diffusion terms in the horizontal (Prandtl approximation), the linear set as solved in Lott *et al.* (2024) can be rewritten in the dimensional form

$$\mathrm{i}kU\hat{u} + \frac{\partial U}{\partial Z}\hat{\boldsymbol{w}} + \mathrm{i}k\frac{\hat{p}}{\rho_\mathrm{r}} = \frac{\partial}{\partial Z}\left\{\underbrace{2lu_*}_{\text{incl } \nu'}\frac{\partial \hat{u}}{\partial Z}\right\} + \mathrm{i}kBf\hat{h} \quad \text{(A.1a)}$$

$$\mathrm{i}kU\hat{b} + \frac{\partial B}{\partial Z}\hat{\boldsymbol{w}} = \frac{\partial}{\partial Z}\left\{lu_*\frac{\partial \hat{b}}{\partial Z} + lb_*\frac{\partial \hat{u}}{\partial Z}\right\}, \quad \text{(A.1b)}$$

$$\mathrm{i}kU\hat{\boldsymbol{w}} + \frac{1}{\rho_\mathrm{r}}\frac{\partial \hat{p}}{\partial Z} - \hat{b} = k^2U^2f\hat{h}, \quad \text{(A.1c)}$$

$$\mathrm{i}k\hat{u} + \frac{\partial \hat{\boldsymbol{w}}}{\partial Z} = -\mathrm{i}kU\,\frac{df}{dZ}\hat{h}, \tag{A.1d}$$

$$\text{where } \hat{\boldsymbol{w}} = \hat{w} - \mathrm{i}kUf\hat{h}, \tag{A.1e}$$

subject to the surface boundary condition ($\hat{u} = \hat{\boldsymbol{w}} = \hat{b} = 0$ in $Z = 0$). In curved coordinates, the mountain forcing is applied via the last terms on the right of Equations (A.1a), (A.1c), and (A.1d).